JOURNAL OF SPACECRAFT AND ROCKETS
Vol. 40, No. 1, January–February 2003

Optimization of Low-Perigee Spacecraft Aerodynamics

D. Stuart Bowman* and Mark J. Lewis†
University of Maryland, College Park, Maryland 20742

An analytical model for rarefied flow is applied to a parameterized aerodynamic configuration of a low-perigee spacecraft. Equations with variable surface reflection conditions are introduced for force calculations on a discretized surface. Optimization is performed with several objective functions: reduced drag, maximum stabilizing moment under pitch and yaw conditions, and maximum lift-to-drag ratio. In each case volume is also maximized. Sample optimizations are studied for two reflection conditions, 100% specular and 75% diffuse. In comparison to a baseline low-perigee spacecraft design, the reduced drag optimized shapes showed an increase in volume and a decrease in drag, although they are aerodynamically unstable for all off-design attitudes. The optimum shape was found to be insensitive to the reflection assumption, although the performance is not. The shapes optimized for maximum stability tend to have reduced volume and significantly increased drag, but are stable for both specular and diffuse reflection conditions. The shapes optimized for maximum lift to drag show that rarefied lift can be increased without a dramatic increase in drag.

Nomenclature

A	=	area, m^2
C	=	shape profile coefficient
C_d	=	drag coefficient
C_l	=	lift coefficient
$\bar{c}$	=	thermal velocity, m/s
D	=	drag, N
e	=	eccentricity, r_z/r_y
F	=	force, N
I_m	=	mass flux, kg/(m$^2 \cdot$ s)
I_n	=	number flux, 1/(m$^2 \cdot$ s)
k	=	lower surface power-law exponent
L	=	lift, N
l	=	upper surface power-law exponent
ℓ	=	length, m
M	=	moment, N $\cdot$ m
m	=	hyperellipse exponent; mass, kg
n	=	hyperellipse exponent; number density, 1/m^3
r	=	radius, m
S	=	side force, N
V	=	velocity magnitude, m/s
x, y, z	=	spacecraft coordinate directions
δ	=	θ'/θ
ϵ	=	$V_{\text{out}}/V_{\text{in}}$
θ	=	angle between V_{in} and surface of incidence
θ'	=	angle between V_{out} and surface of reflection
ξ	=	percent specular reflection
ρ	=	mass density, kg/m^3
ψ	=	angle between a surface plane and the y-axis

Subscripts

base	=	base dimension of vehicle
body	=	geospace electrodynamic connections (GEC) cylinder
complete	=	final form of equations
diff	=	diffuse reflection
in	=	incoming to surface
l	=	lower surface
nose	=	GEC truncated cone portion
out	=	outbound from surface
pitch	=	pitch motion
S/C	=	spacecraft
u	=	upper surface
x, y, z	=	spacecraft coordinate directions
0–8	=	coefficients

Received 15 June 2001; revision received 7 June 2002; accepted for publication 16 September 2002. Copyright © 2002 by the American Institute of Aeronautics and Astronautics, Inc. All rights reserved. Copies of this paper may be made for personal or internal use, on condition that the copier pay the $10.00 per-copy fee to the Copyright Clearance Center, Inc., 222 Rosewood Drive, Danvers, MA 01923; include the code 0022-4650/03 $10.00 in correspondence with the CCC.

*Graduate Research Assistant, Department of Aerospace Engineering; dsbowman@eng.umd.edu. Student Member AIAA.

†Professor, Department of Aerospace Engineering; lewis@eng.umd.edu. Associate Fellow AIAA.

Introduction

THERE are numerous scientific questions yet to be explored regarding Earth's upper atmosphere. Included in these questions are the influence of electromagnetic occurrences and time/space variations of atmospheric constituents in this upper region. Much data have been collected throughout the years by various sounding rocket missions,[1,2] satellite observations,[1,3–5] and mass spectrometer/incoherent scatter measurements,[5–7] which have provided the scientific community with a substantial, but incomplete, understanding of the near-space atmosphere. This understanding is limited because most of the data has been collected during single passes through the atmosphere (as with the rocket missions) that could not accurately measure spatial and time gradients, or obtained remotely via satellite observations with limited resolution.

Recently, a new class of science satellites that are designed to skim through the upper atmosphere have been proposed, including the NASA Goddard Space Flight Center's Geospace Electrodynamic Connections (GEC).[8] These "dipper" spacecraft use a low-perigee orbit similar to the one shown in Fig. 1 to enter into the upper atmosphere for a short duration of the orbit period. The spacecraft perform various in situ scientific objectives before exiting the atmosphere and continuing toward apogee. Because the trajectory repeats itself, the spacecraft are able to provide a consistent, predictable means of studying the Earth's upper atmosphere.

These low-perigee spacecraft missions will encounter aerodynamic forces as the spacecraft enters the rarefied flow regime of the Earth's upper atmosphere. The forces, which are small relative to low-atmosphere vehicles, can have a positive or negative effect on the performance, lifetime, and stability of the vehicle depending on its perigee and apogee altitudes and the mission objectives. Drag forces change the perigee velocity causing, among other influences, the decrease of orbit eccentricity and/or the use of fuel to maintain orbit. Yaw forces could contribute to stability concerns by generating unwanted moments. These effects suggest that there is value to properly designing the aerodynamic performance of dipper spacecraft.

There has been extensive work in seeking optimal shapes for continuum flow but much less in the rarefied regime. Carter[9] sought

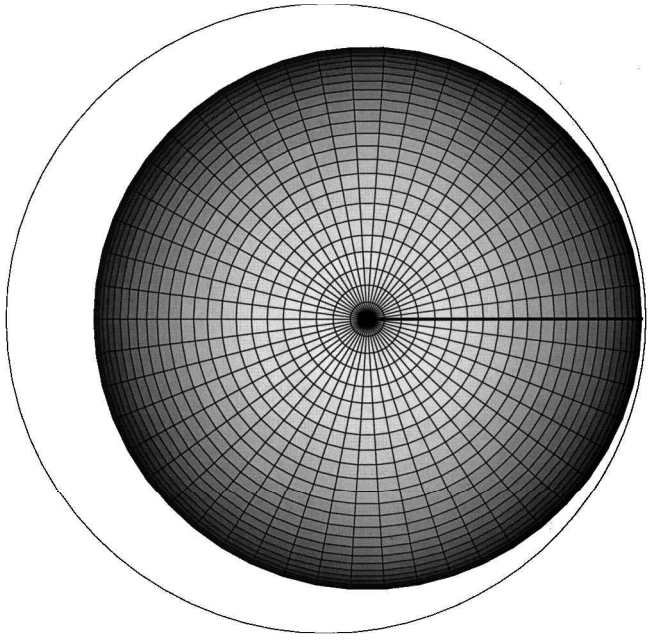

Fig. 1 Scale representation of the low-perigee orbit about a spherical Earth.

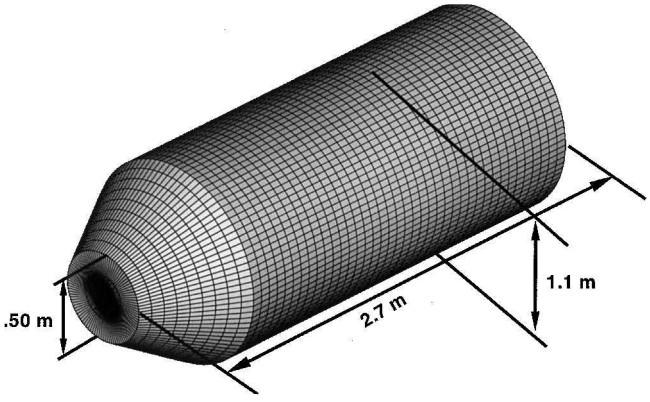

Fig. 2 GEC geometry used for comparison.

axisymmetric minimum drag missile nose shapes using kinetic theory and surfaces of varying roughness. His work produced numerical solutions that varied based on the surface roughness assumption. A continuation of Carter's work by Tan[10] provided minimum drag analytical solutions that approached power-law shapes.

Multiple authors[11,12] have explored the concept of upper atmosphere aerodynamic maneuvering. Lewis[13] has suggested that plane changes may be possible through proper spacecraft design by providing an appropriate lift-to-drag ratio (L/D). At an L/D in excess of unity, the aerodynamic plane change becomes advantageous over pure propulsive plane change options. The suggested sequence is to drop the spacecraft out of orbit into the upper atmosphere just far enough that sufficient lift is available for a plane change. Following the maneuver, the spacecraft is boosted back out to its original orbit. A new class of high-lift spacecraft designs would be required to exploit this type of maneuver.

This current work attempts to address the aerodynamic design issues faced within the rarefied environment of the Earth's upper atmosphere using the computational solution of an analytical geometry model. A numerical optimizer is employed to analyze a 13-design-variable geometry for various objective functions and for a range of gas–surface accommodation assumptions.

The baseline shape for the NASA Goddard Space Flight Center's GEC mission is used as a benchmark against which to compare the optimized geometries. This mission seeks to study the ionosphere's electrodynamic environment by orbiting a cluster of four spacecraft on a trajectory that will continually bring the spacecraft into contact with the Earth's ionosphere. The baseline GEC geometry was designed without significant aerodynamic considerations and consists of a cylinder body with a truncated cone for the nose. The geometric properties are listed in Table 1 with the full geometry shown in Fig. 2. The base of this geometry is open (for instrument placement) as is the geometry used for the optimizations. The perigee of this orbit is 130 km ($\rho = 6.2 \times 10^{-9}$ kg/m^3), which will be used as the baseline minimum altitude in this work.

Table 1 Properties of the GEC geometry

Property	Value
ℓ_{body}, m	2.20
ℓ_{nose}, m	0.50
r_{body}, m	0.55
r_{nose}, m	0.25
Surface area, m^2	9.25
Volume, m^3	2.35
$\text{Drag}_{spec/diff}$, N	0.3273/0.5441
$M_{restoring,spec/diff}$, N · m	7.2463e−3/−7.9798e−2

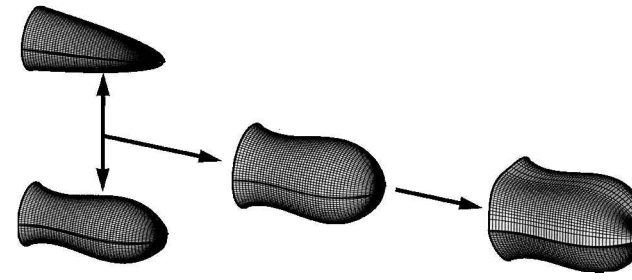

Fig. 3 Geometry evolution from multiple desired shapes to one.

Geometry Model

A primary concern for low-perigee spacecraft is the drag force incurred by entering the atmosphere and the possibly destabilizing moments generated by the aerodynamic forces. Previous work[9,10] has shown that a minimum drag body can be approximated by a three-quarter power-law shape assuming specular reflection; this result is the same as for hypersonic continuum flow. However, a monotonic power-law shape may have destabilizing moments at off-design. For this work our axisymmetric third-order polynomial shape was chosen because of its ability to produce a flare at its end. Under straight and level flight conditions, the spacecraft's flare region will have equal particle impingement on all surfaces, and the moments will be balanced. However, as the spacecraft enters a pitch or yaw orientation, the flared portion will become more exposed to the flow on one side and less exposed to the flow on the other, creating a restoring moment. To approximate both low-drag and highly stable shapes, the geometric function retained both power-law and polynomial terms by linear combination of the generating equations. To increase the diversity of shapes available in the geometry model, a superellipse[14] cross section has been used to allow nonaxisymmetric shapes. This complete geometry evolution is shown in Fig. 3.

The profile of the spacecraft shape is, thus, defined by the following equations:

$$y_u = C_1 x^3 + C_2 x^2 + C_3 x + C_0 + C_4 x^k \tag{1}$$

$$y_l = C_5 x^3 + C_6 x^2 + C_7 x + C_0 + C_8 x^l \tag{2}$$

The upper and lower surface powers and scaling coefficients are independent, thereby affording the greatest flexibility in the geometry model. For the cases studied here, the exponents l and k are bounded such that $0 < l, k \leq 1$, and C_0 is fixed at a value of 0.25 to provide a flat nose for instrument mounting (similar to the GEC geometry).

The cross-section shape is composed of an upper and lower surface, which are coupled only in their width. The superellipse formulation for the cross-sectional shape is

$$z_{u,l} = r_{z_{u,l}} (\sin\theta)^{(m,n)} \tag{3}$$

$$y_{u,l} = r_{y_{u,l}}(\cos\theta)^{(m,n)} \tag{4}$$

where m is the power for the upper surface u and n is the power for the lower surface l. These functions provide a large range of practical cross-section shapes; exponents $m, n = 1$ give circular shapes; $m, n < 1$ give squarelike shapes; $m, n > 1$ give diamondlike shapes. Also, they automatically cluster points in regions of curvature, which provides a better analytical mesh for force calculation. An eccentricity variable is used to allow r_z and r_y to vary as a proportion, similar to the relationship of the semimajor and semiminor axes of an ellipse. The length of the spacecraft is set to a constant of 3 m for all optimizations (comparable to an early concept for GEC). Overall, there are 13 shape-controlling variables, which are as follows: 1) upper surface profile, C_{1-4} and k; 2) lower surface profile, C_{5-8} and l; and 3) cross section, m, n, and e. These variables provide a large range of possible spacecraft shapes, thereby allowing great flexibility for the optimization.

Aerodynamic Model

Analytical solutions to pressure force in rarefied flow were applied to provide reasonable optimization run times. The model is similar to that of Bird,[15] but implementation of an analytic solution saves much computing time when compared with computational approaches such as direct simulation, which seeks to model individual flow molecules.

With large mean free path, force per unit area is taken as a function of surface angle only. The drag and lift per unit area (Fig. 4) are

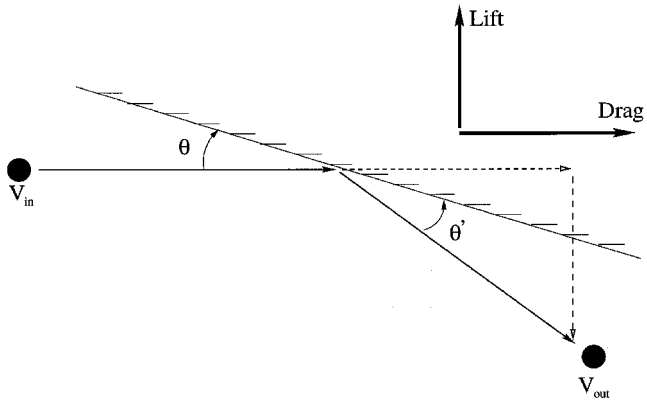

Fig. 4 Physical representation of aerodynamic model.

$$\frac{D}{A} = \left[\frac{\mathrm{d}(mV)}{\mathrm{d}t}\right]_{\text{in}} - \left[\frac{\mathrm{d}(mV)}{\mathrm{d}t}\right]_{\text{out}} \cos(\theta + \theta') \tag{5}$$

$$\frac{L}{A} = \left[\frac{\mathrm{d}(mV)}{\mathrm{d}t}\right]_{\text{out}} \sin(\theta + \theta') \tag{6}$$

The flux of molecules to the surface is decomposed into a convective component and a thermal impingement rate, $I_n = n(\bar{c}/4)$, where $\bar{c}$ is the thermal velocity component and n is the molecular number density.[16] The flux due to thermal velocity is nearly negligible at all but small angles of impingement due to the comparatively large magnitude of the spacecraft velocity, that is, $V_{\text{in}} \gg \bar{c}$. Under these conditions, flux can be simplified by linearly summing the thermal and freestream flux:

$$I_m = \rho[V_{\text{in}} \sin\theta + (\bar{c}/4)] \tag{7}$$

where ρ is the mass density ($\rho = nm$) and $\sin\theta$ is the unit capture area of a surface inclined at angle θ to the flow. Then, three-dimensional equations for aerodynamic forces can be written as

$$D/A = I_m V_{\text{in}}\{1 - \epsilon\cos[\theta(1+\delta)]\} \tag{8}$$

$$L/A = I_m V_{\text{in}}\,\epsilon\sin[\theta(1+\delta)]\cos(\psi) \tag{9}$$

$$S/A = I_m V_{\text{in}}\,\epsilon\sin[\theta(1+\delta)]\sin(\psi) \tag{10}$$

where ψ is the angle between a surface and the y axis and ϵ and δ are particle accommodation coefficients defined as the rebound-to-incoming velocity and angle ratios, respectively. For specular reflection, ϵ and δ are unity, and for complete accommodation with no rebound, ϵ and δ are zero.

Diffuse Scattering

Actual rarefied surface interactions will include at least some diffuse reflection. To include this specifically, a modification is introduced to the surface force calculation. A diffuse surface reflection can be thought of as the release of a particle that hit at some previous time and stuck for a while. The velocity of the particle is, therefore, at most, only mildly related to the incoming particle velocity.[15] Previous work[17,18] has reported that the scattering pattern of a diffuse reflection is, on a limited scale, proportional to a polarly plotted trigonometric distribution that is symmetric about the surface normal. This distribution, which has previously been used in some Monte Carlo simulation schemes,[19] is shown in Fig. 5. In this work, a sine distribution is used to show possible solutions under the diffuse assumption.

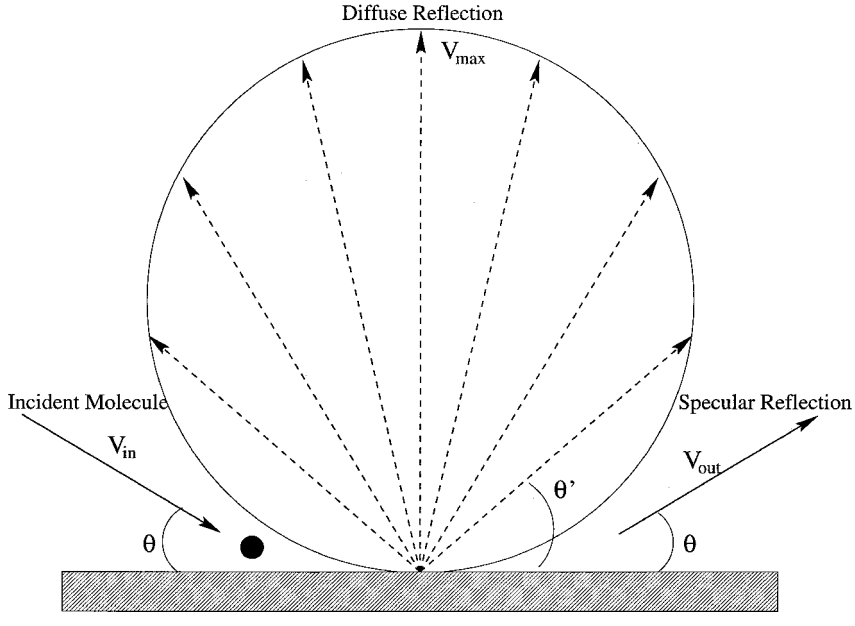

Fig. 5 Sine law representation of the diffuse reflection possiblities (from Ref. 18).

From Eq. (8) on, the term $\theta(1+\delta)$ is rewritten as $(\theta+\theta')$, where θ' is still the molecule rebound angle as before. Then, ϵ is redefined as a function of velocity from the polar sine distribution

$$\epsilon_{\text{diff}} = (V_{\max}/V_{\text{in}})\sin\theta' \tag{11}$$

where $V_{\max}$ is the maximum rebound velocity and $0 \le \theta' \le \pi$. The velocity ratio term is generally a function of surface temperature[9] but can be approximately determined by integrating over the lobular reflection distribution from 0 to π. Normalizing to the interval length provides a mean rebound velocity ratio of 2/3. This ratio is used as a constant in this work. When Eq. (11) is used and the diffuse reflection is restricted to the special case of a normal component only ($\theta' = \pi/2$), Eqs. (8–10) can be rewritten as

$$D/A|_{\text{diff}} = I_m V_{\text{in}}\left(1 + \tfrac{2}{3}\sin\theta\right) \tag{12}$$

$$L/A|_{\text{diff}} = I_m V_{\text{in}}\tfrac{2}{3}\cos\theta\sin\psi \tag{13}$$

$$S/A|_{\text{diff}} = I_m V_{\text{in}}\tfrac{2}{3}\cos\theta\cos\psi \tag{14}$$

Complete Equations

To consider a large range of accommodation behaviors, the full set of equations is formed from a linear addition of Eqs. (8–10) and the diffuse reflection equations (12–14). A coefficient ξ is used to determine the percent of specular reflection during a simulation

$$F_{x,y,z}/A|_{\text{complete}} = \xi(F_{x,y,z}/A)|_{\text{spec}} + (1-\xi)(F_{x,y,z}/A)|_{\text{diff}} \tag{15}$$

These three force equations can be easily employed in the computation of aerodynamic forces on a vehicle with a discretized surface, all with very little computational expense. The coefficients for the geometries presented here will be referenced to base area A_{base} as

$$C_{d,\text{S/C}} = 2D/\rho V^2 A_{\text{base}}, \qquad C_{l,\text{S/C}} = 2L/\rho V^2 A_{\text{base}} \tag{16}$$

Negative Angle Surfaces

The equations derived assume an incident angle $0 \le \theta \le 90$ deg. However, this surface angle is not always the case with the polynomial geometry because the angle between the velocity vector and the surface can be negative. Because the impingement due to thermal velocity component is in all directions, there will be some small fraction of impingement at moderate negative angles. To account for this impingement on negative surfaces, a triangle is formed using V_{in} and the thermal velocity component assuming that the two are perpendicular vectors. The angle between the resulting hypotenuse and V_{in} is considered the most negative angle on which impingement can occur, and appropriate calculations are made based on that limiting angle. Secondary impingement between negative surfaces and positive surfaces is neglected.

Optimization

This optimization is carried out using Design Optimization Tools, version 4.0, by VMA Engineering.[20] The constrained solution is found using the modified method of feasible directions.[21] Optimizations have been carried out with the 13-design-variable geometry using a specular reflection assumption ($\xi = 1$) and 75% diffuse reflection assumption ($\xi = 0.25$). Actual on-orbit reflection conditions are difficult to predict. These two chosen do not represent believed on-orbit conditions, rather these have been chosen to show solution dependence on the reflection assumption and to help bound the problem.

Optimization Constraints

This design problem has constraints that are imposed by engineering practicalities. Because these low-perigee spacecraft are envisioned to be used in a constellation (for simultaneous time and space measurement opportunities), they are designed so that multiple spacecraft can fit within a single launch shroud. In the case of the GEC mission, four identical spacecraft are currently expected to launch together in a Delta shroud. If the GEC designs are packaged side-by-side, the maximum volume for one GEC spacecraft is a "pie-shaped" prismatic space in which one GEC spacecraft must fit, as shown in Fig. 6a. This volume is used to evaluate the distances between the launch shroud and the vehicle in five separate locations, as shown in Fig. 6b.

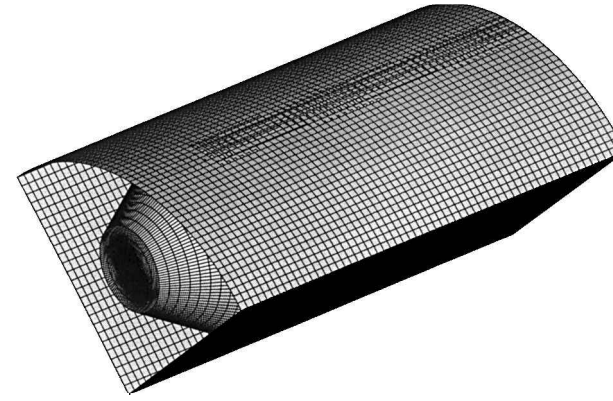

a) GEC launch vehicle space

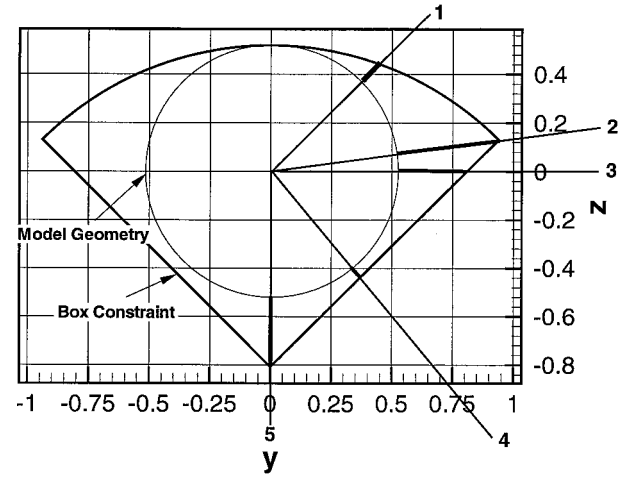

b) Five launch vehicle constraints

Fig. 6 Launch shroud vehicle constraints.

The second geometric constraint involves internal component placement and ensuring that there is adequate volume in the correct locations for certain basic components. Currently, only the fuel tank is being considered because it is the largest and highest mass internal piece of GEC. The GEC tank is approximated by a slightly elongated sphere of radius 0.5 m and is assumed to be located 0.1 m behind the nose and on the longitudinal axis. Fuel tank dimensions are checked at three points on the geometry (upper surface, lower surface, and width) to ensure vehicle feasibility.

Because of the nature of the third-order polynomial used, the upper and lower surfaces may generate nonuseful geometries with crossing surfaces, as shown in Fig. 7a. To ensure that this situation was not considered a valid design, two constraints were calculated such that the minimum point on the profile of the upper and lower surfaces had to be greater and less than zero, respectively. Next, two more constraints were set to ensure that the end of the upper and lower surfaces were greater than and less than zero, respectively. An example of these four points is shown in Fig. 7b.

Objective Functions

There are multiple aspects of this geometry model that could be explored. Of primary initial interest were those shapes that produce minimum rarefied aerodynamic drag. Also of interest were shapes that have restoring moments during off-design orientations. The results of the following three optimization objectives will be presented here as maximizations: 1) drag reduction study, volume/drag; 2) aerodynamic stability study,

$$\text{volume} \times \sum_{i=1}^{3} \text{moment}_i$$

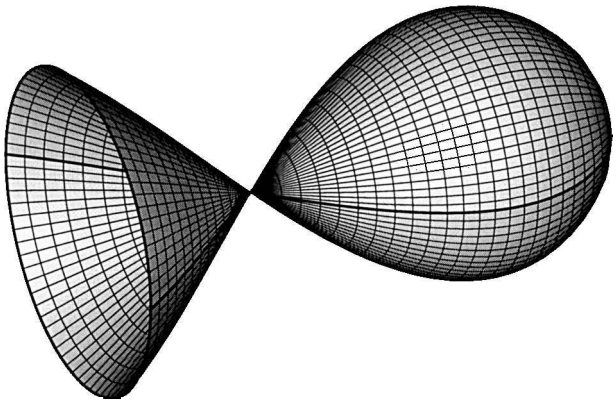

a) Crossing surfaces

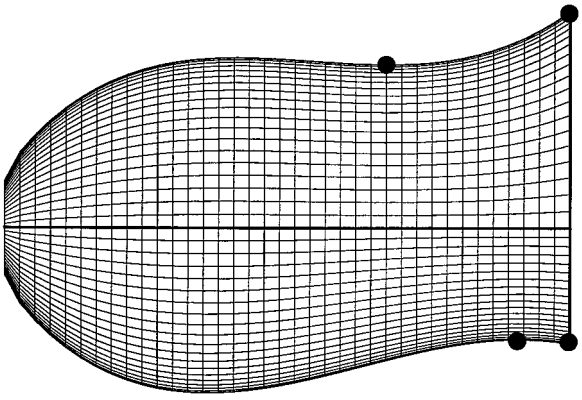

b) Four flare evaluation points

Fig. 7 Spacecraft flare constraints.

and 3) lift and drag study, volume × lift/drag. Stability is determined by calculating the moments acting on the spacecraft under three off-design conditions: positive pitch, negative pitch, and positive yaw (which is the same as negative yaw for these geometries). Moments are summed about the spacecraft center of gravity, which is different for each design point.[22] A somewhat arbitrary worst-case off-design scenario of 5 deg from the velocity vector was used in each condition.

Optimization Results

Before beginning the full 13-variable optimizations, four reduced design variable studies were performed using the specular reflection assumption and all of the constraints (to generate feasible designs with which to initialize the full optimizations). These studies were as follows: First, an axisymmetric power-law shape study used two design variables, C_4 and k, to generate power-law shapes with the same upper and lower surface. A systematic search of the reduced design space was used. Of the 1600 designs tried in this space, only 1 design was feasible (Fig. 8a). Second, an axisymmetric polynomial shape study used three design variables, C_1–C_3, to generate polynomial shapes with the same upper and lower surfaces. The design space was split into 64,000 equally spaced designs. Of these, only three designs were feasible (Fig. 8b–8d). Third, zero-lift shapes in which seven design variables, C_{1-4}, k, e, and m, were used to provide designs in which the upper and lower surfaces were the same. These shapes were optimized using the reduced drag objective function and a specular reflection assumption (Figs. 8e and 8f). Fourth, maximum volume shapes in which seven design variables, C_4, C_8, k, l, e, m, and n, were used to generate power-law designs that had fully separate upper and lower surfaces. This shape was optimized by maximizing volume (Fig. 8g).

Reduced Drag Study

For the specular portion of this study, 10 separate initial designs were used. Seven from the initial studies and three additional initial designs were also used. Each optimization solution had very different objective function values, suggesting that the reduced drag design space is not flat. The best constrained solution was the optimum from the no-lift study (design 5 in Fig. 8). This optimum vehicle shape, shown in Fig. 9, is not axisymmetric or cylindrical like the GEC design. Nearly all of the drag is accumulated on the nose by the flat, forward-facing surface, while the sides are aligned nearly parallel to the molecule flow (minimizing impingement on the sides of the shape). Compared to the GEC design, this shape has 38% less drag, 5% more volume, and 7.5% more surface area. Note that this design appears to be cylindrical, but the variables m and n actually have values 30% greater than unity.

The diffuse accommodation optimization used designs 1–7 plus an additional eighth initial design point. Even though the design space has changed due to the change in reflection assumption, design 5 again produced the best objective value. As with the specular

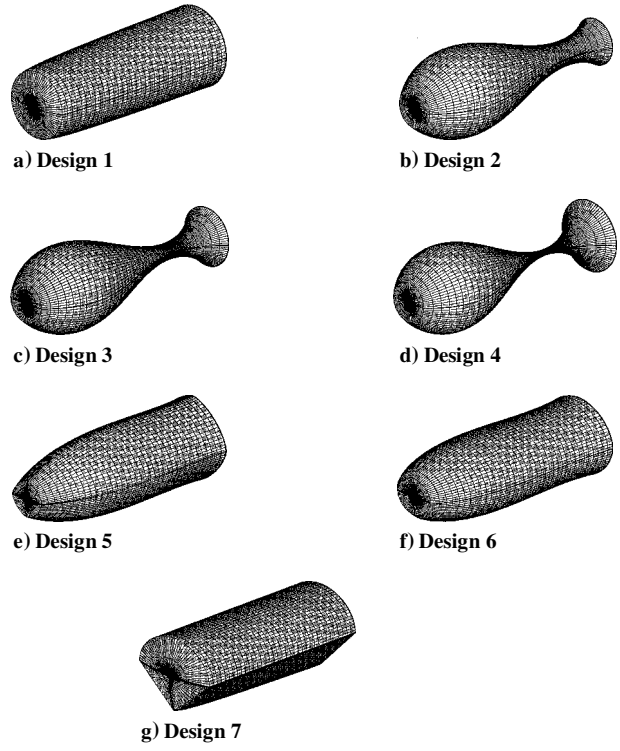

a) Design 1 b) Design 2 c) Design 3 d) Design 4 e) Design 5 f) Design 6 g) Design 7

Fig. 8 Reduced design variable optimization results using specular reflection conditions.

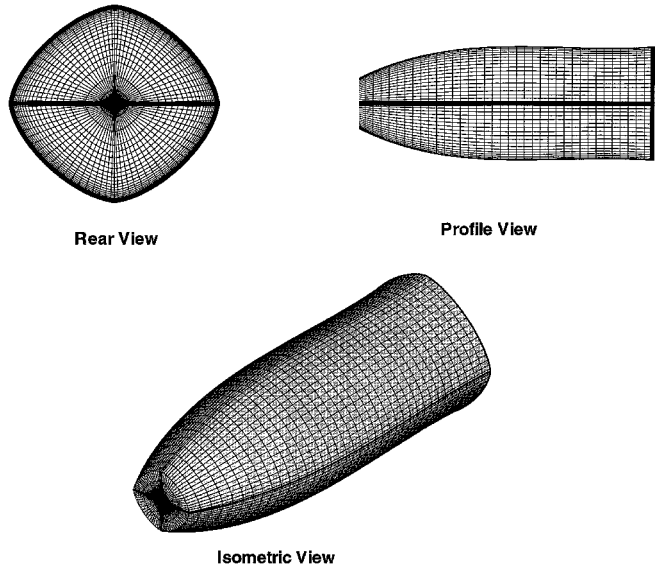

Fig. 9 Reduced drag optimized geometry (design 5) using specular reflection conditions.

Table 2 Optimum reduced drag designs

Parameter	Specular	Diffuse
	Upper surface	
C_1	$3.939E-02$	$3.755E-02$
C_2	-0.2500	-0.2502
C_3	0.4886	0.4892
C_4	$1.779E-02$	$1.8372E-02$
k	0.9615	0.9615
	Lower surface	
C_5	$3.939E-02$	$3.877E-02$
C_6	-0.2500	-0.2500
C_7	0.4886	0.4887
C_8	$1.779E-02$	$1.793E-02$
l	0.9615	0.9615
	Cross-section	
e	0.9442	0.9442
m	1.3031	1.3031
n	1.3031	1.3031
	Vehicle parameters	
Drag, N	0.2038	0.4606
Lift, N	0.0000	$2.470E-03$
Yaw, N	0.0000	0.0000
M_{pitch}, N · m	0.0000	$-2.5034E-09$
$C_{\text{d,S/C}}$	1.0256	2.6702
L/D	0.0000	$5.362E-03$
Volume, m^3	2.4679	2.3761

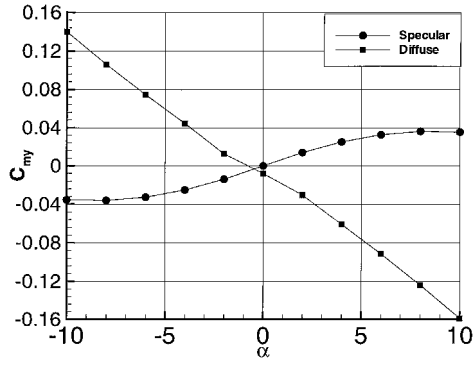

Fig. 10 Pitching moment coefficient curves for both reduced drag optimized shapes.

result, this solution is a constrained optimum, which is why the optimum point changed very little between the specular and diffuse reflection assumption.

The full aerodynamic performance of both optimal shapes is given in Table 2. There is a slight difference in the designs, which is on the order of numerical error. As noted, in both the specular and diffuse cases the volume is a few percent greater than the baseline design. However, drag for both cases is significantly less than the baseline shape.

Figure 10 shows pitching moment coefficient curves for the specularly and diffusely optimized spacecraft. Because this shape is essentially a zero lift body, the curves are symmetric about the 0-deg angle of attack. The specularly optimized shape is marginally stable at 0 deg and unstable at all other points plotted. Conversely, the spacecraft designed under the diffuse reflection assumption is stable across the entire angle-of-attack range. Thus, the same design changes stability characteristics based on reflection assumption.

Aerodynamic Stability Study

The goal of this portion of the study was to produce designs that have restoring moments under conditions of positive and negative pitch and positive and negative yaw. Three more constraints were added in this optimization to force the optimizer to seek designs with the correct moment directions. For the specular study, 10 initial designs are used. The optimum configuration, shown in Fig. 11, has 20% less volume than GEC, 73% more drag than GEC, 1% less surface area than GEC, and is elliptical in cross-sectional, shape.

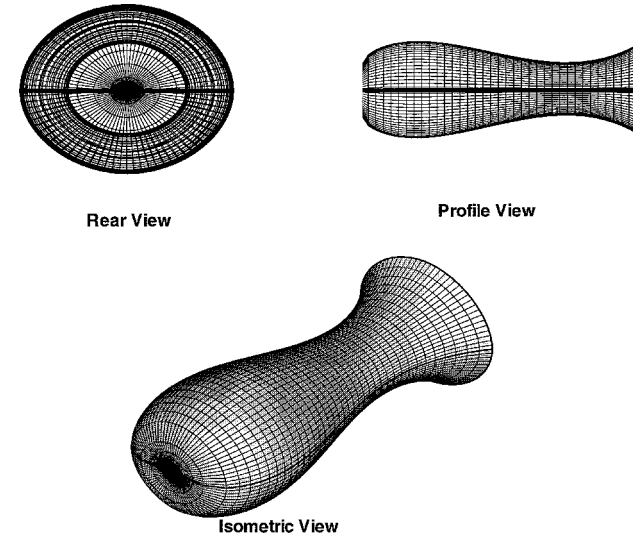

Fig. 11 Stability optimized geometry using specular reflection conditions.

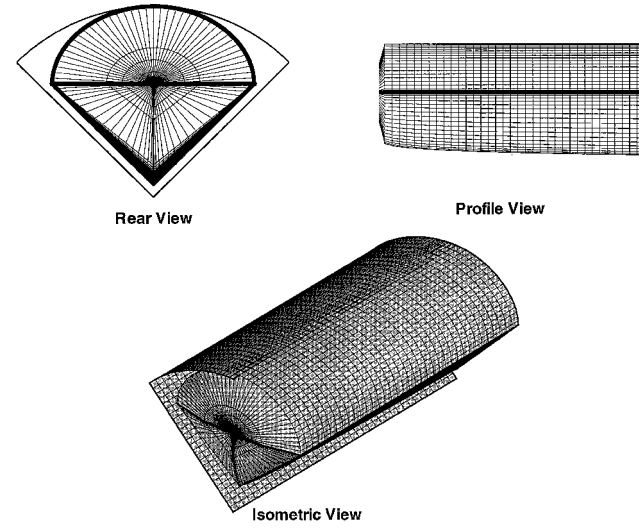

Fig. 12 Stability optimized geometry using diffuse reflection conditions.

The optimizer sought this lower eccentricity value because it causes the surface area to increase and, thus, the moments to increase.

The diffuse optimizations for stability used eight initial designs. The optimum configuration is shown in Fig. 12 and was design 7 from the reduced design variable study. This shape has 39% more volume than GEC, 43% more drag than GEC, and 33% more surface area than GEC.

Note that design 7 did not produce a feasible design under specular reflection conditions (due to the additional moment constraints). Yet, under these diffuse conditions, design 7 actually produced the highest objective value due in large part to its high volume. This result is the same phenomenon seen in the reduced drag study, in which a given configuration was unstable for specular reflection but stable for diffuse reflection. However, unlike the reduced drag optimization, the reflection assumption has dramatically influenced the optimum point in the stability design space. The design variable values and aerodynamic data for both the specular and diffuse optima are listed in Table 3.

Figure 13 shows the pitching moment curves for the specularly and diffusely optimized configuration. When this curve is examined, note that both shapes are stable across the range of off-design orientations. This performance is significantly better than the drag optimized geometries.

Table 3 Optimum stability designs

Parameter	Specular	Diffuse
	Upper surface	
C_1	9.9152E−02	0.0000
C_2	−0.3703	0.0000
C_3	3.947E−02	0.0000
C_4	0.4638	0.2877
k	0.5108	0.000
	Lower surface	
C_5	1.011E−01	0.0000
C_6	−0.3743	0.0000
C_7	0.5470	0.0000
C_8	0.4544	0.4006
l	0.5126	0.9178
	Cross section	
e	0.8076	0.7738
m	1.0502	1.0172
n	1.0503	1.9945
	Vehicle parameters	
Drag, N	0.5657	0.7780
Lift, N	−6.521E−04	1.348E−02
Yaw, N	−4.980E−09	7.598E−09
$M_{\text{pitch},0\ \text{deg}}$, N · m	−8.7050E−03	9.5403E−03
$M_{\text{pitch},5\ \text{deg}}$, N · m	−7.156E−02	−4.695E−02
$M_{\text{pitch},-5\ \text{deg}}$, N · m	5.405E−02	8.067E−02
$M_{\text{yaw},5\ \text{deg}}$, N · m	−5.165E−02	−5.926E−02
$C_{d,\text{S/C}}$	2.7213	3.6240
L/D	−1.152E−03	1.732E−02
Volume, m^3	1.8718	3.2704

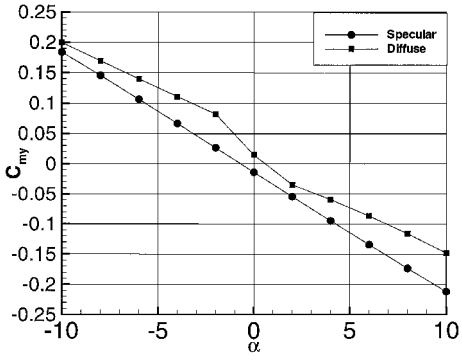

Fig. 13 Pitching moment coefficient curves for both stability optimized shapes.

Maximum *L/D* Study

This portion of the optimization study addresses the feasibility of the L/D goal set forth by Lewis[13] of obtaining an L/D of unity. With no molecule reflection (a highly unlikely occurance), lift is not possible; with modest accommodation (more likely) it was of interest to seek maximum L/D, or at least $L/D >$ unity. For the specular portion of this study, 10 designs are used, with the best solution shown in Fig. 14. This design has 19% less volume than GEC, 30% less drag than GEC, and 3% less surface area than GEC.

The diffuse optimization was carried out using the standard seven initial designs with three additional designs. The optimum configuration is shown in Fig. 15. Compared to the GEC design, this shape has less than 1% increase in volume, approximately a 1% increase in drag, and an 8% increase in surface area. Note that this design did not have the best L/D ratio of the set. The best L/D ratio was just over 0.1, but this configuration had a volume of 1.5 m^3 which forced the objective value to be low. The best diffuse-reflection design has much better volume than the specular counterpart, but the actual L/D ratio is 30% lower. The increased volume is reasonable given that the diffuse optimal solution has a much more blunt nose than does the specular best shape.

The design variables and performance information for both optimal shapes are given in Table 4. Noted that for both shapes the L/D is an order of magnitude below the design goal of unity. However, the L/D ratios are in a similar range to each other. This result does not mean that $L/D > 1.0$ is unobtainable, only that it is not achievable with this class of geometries.

Table 4 Optimum *L/D* designs

Parameter	Specular	Diffuse
	Upper surface	
C_1	5.968E−02	1.006E−03
C_2	−0.3526	−2.470E−02
C_3	0.5146	3.361E−02
C_4	5.371E−02	0.2439
k	0.9554	7.41E−02
	Lower surface	
C_5	4.586E−03	−3.174E−03
C_6	−0.2482	−0.1207
C_7	0.5470	6.01E−02
C_8	7.780E−02	0.3669
l	0.9596	0.9178
	Cross section	
e	0.9036	0.9163
m	1.4076	1.0168
n	1.2152	0.9378
	Vehicle parameters	
Drag, N	0.2294	0.5508
Lift, N	2.774E−02	4.065E−02
Yaw, N	3.359E−09	−2.505E−06
M_{pitch}, N · m	2.075E−02	1.869E−02
$C_{d,\text{S/C}}$	5.1923	5.5267
L/D	0.1209	7.380E−02
Volume, m^3	1.8904	2.3435

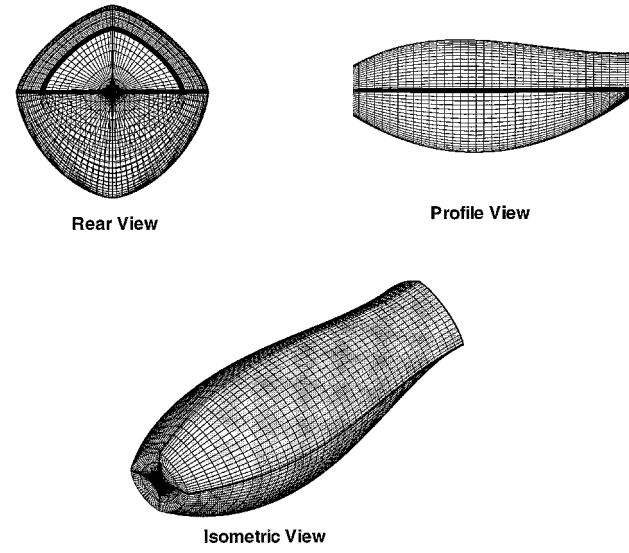

Fig. 14 *L/D* optimized geometry using specular reflection conditions.

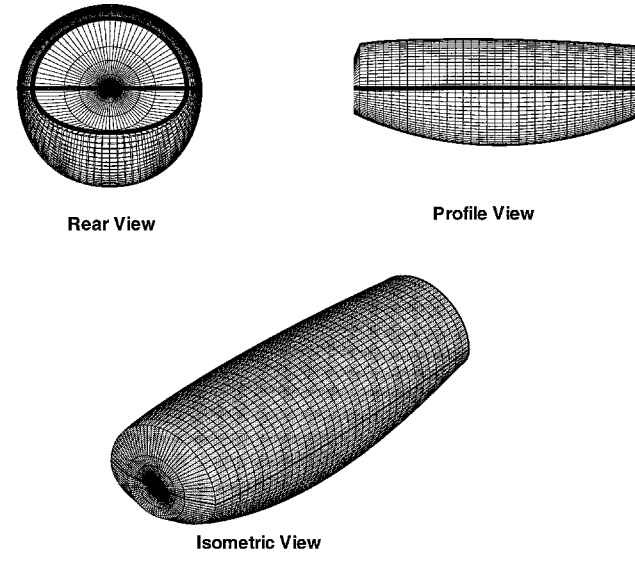

Fig. 15 *L/D* optimized geometry using diffuse reflection conditions.

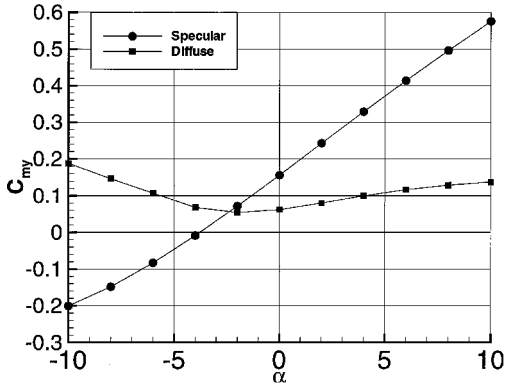

Fig. 16 Pitching moment coefficient curves for both *L/D* optimized shapes.

Figure 16 shows the pitching moment coefficient for the specularly and diffusely optimized L/D spacecraft. The trim angle for the specular configuration is near the zero-lift point. This lifting body is marginally stable at trim conditions; for all other attitudes this spacecraft is unstable. The diffuse curve maintains positive pitching coefficients. This vehicle always has a positive pitching moment acting on it and is aerodynamically unstable for all attitudes. However, the practical consequence of these moments will depend on the time constants and moment magnitude.

Conclusions

This study has sought to explore the aerodynamic design space for low-perigee spacecraft. An analytical aerodynamic model has been applied to a parameterized aerodynamic configuration for low-perigee spacecraft. The equations contain variable surface reflection conditions and were solved on a discretized body. Optimization of the spacecraft shape has been performed using two different reflection conditions and three different objective functions.

Results of this study show that with this geometry model, significant drag reduction across the reflection assumption range is possible (compared to the baseline shape). The best shape was zero lift, noncylindrical, and had higher volume and surface area than the GEC design. This was true for both reflection conditions explored and, in fact, the best shape was only a weak function of the reflection assumption. There are, however, moment production concerns with these shapes that warrant further study before production.

This geometry model does allow generation of aerodynamically stable configurations across the reflection range explored, and the moment coefficient values were of similar order. However, the shapes changed dramatically due to reflection condition and showed that aerodynamic stability is a strong function of reflection assumption. Also, significant drag and volume penalties exist for these stable shapes. To cancel these penalties, other stability methods (reaction wheels for instance) should be considered in the design process.

The L/D goals set forth are not attainable with this geometry model or within these constraints. However, note that these shapes did not change significantly based on the reflection assumption, generated lift without drag penalty, and had similar maximum L/D values across the reflection range explored. These shapes also generate aerodynamic stability concerns. Further study using different geometries is necessary to investigate fully the feasibility of aeromanuevers for spacecraft.

Acknowledgments

This work has been supported by the NASA Goddard Space Flight Center (NASA Grant NAG 59890). The authors thank Jan Gervin, Frederico Herrero, Shane Hynes, Joseph M. Grebowsky, Dominic Manzer, and Gerald J. LeBeau (NASA Johnson Space Center) for their contributions to this work. The support of Mary DiJoseph and Paul Buchanan is also gratefully acknowledged.

References

[1] *U.S. Standard Atmosphere, 1976*, National Oceanic and Atmospheric Administration, NASA, U.S. Air Force, Washington, DC, 1976, pp. 21–32.

[2] Eriksen, T., Hoppe, U.-P., Thrane, E. V., and Blix, T. A., "Rocketborne Rayleigh Lidar for In Situ Measurements of Neutral Atmospheric Density," *Applied Optics*, Vol. 38, No. 12, 1999, pp. 2605–2613.

[3] Broglio, L., Arduini C., Buongiorno, C., Ponzi, U., and Ravelli, G., "Diurnal Density Variations Measured by the San Marco 3 Satellite in the Equatorial Atmosphere," *Journal of Geophysical Research*, Vol. 81, No. 7, 1976, pp. 1335–1349.

[4] Chandra, S., and Spencer, N. W., "Exospheric Temperature Inferred from the Aeros-A Neutral Composition Measurement," *Journal of Geophysical Research*, Vol. 80, No. 25, 1975, pp. 3615–3621.

[5] Hedin, A. E., Maye, H. G., Reber, C. A., Spencer, N. W., and Carignan, G. R., "Empirical Model of Global Thermospheric Temperature and Composition Based on Data from the Ogo 6 Quadrapole Mass Spectrometer," *Journal of Geophysical Research*, Vol. 79, No. 1, 1974, pp. 215–225.

[6] Hedin, A. E., Reber, C. A., Newton, G. P., Spencer, N. W., Brinton, H. C., and Mayr, H. G., "A Global Thermospheric Model Based on Mass Spectrometer and Incoherent Scatter Data MSIS II—Composition," *Journal of Geophysical Research*, Vol. 82, June 1977, pp. 2148–2156.

[7] Hedin, A. E., "Extension of the MSIS Thermosphere Model into the Middle and Lower Atmosphere, *Journal of Geophysical Research*, Vol. 96, No. A2, 1991, pp. 1159–1172.

[8] "Understanding Plasma Interactions with the Atmosphere: The Geospace Electrodynamics Connection (GEC) Mission," NASA TM-2001-209980, NASA Goddard Space Flight Center, July 2001.

[9] Carter, W. J., "Optimum Nose Shapes for Missiles in the Superaerodynamic Region," *Journal of the Aeronautical Sciences*, Vol. 7, July 1957, pp. 527–532.

[10] Tan, H. S., "On Optimum Nose Curves for Superaerodynamic Missiles," *Journal of the Aeronautical Sciences*, Vol. 25, No. 4, 1958, pp. 263–264.

[11] Lees, L., Hartwig, F. W., and Cohen, C. B., "Use of Aerodynamic Lift During Entry into the Earth's Atmosphere," *ARS Journal*, Vol. 29, No. 9, 1959, pp. 633–641.

[12] London, H. S., "Change of Satellite Orbit Plane by Aerodynamic Heating," *Journal of the Aerospace Sciences*, Vol. 29, No. 3, 1962, pp. 323–332.

[13] Lewis, M. J., "Aerodynamic Maneuvering for Stability and Control of Low-perigee Satellites," American Astronautical Society, AAS Paper 01-239, Feb. 2001.

[14] Gardner, M., *Mathematical Carnival*, 1st ed., Vintage Books, New York, 1965, pp. 54–63.

[15] Bird, G. A., *Molecular Gas Dynamics and the Direct Simulation of Gas Flows*, Clarendon, New York, 1994, p. 257.

[16] Vincenti, W. G., and Kruger, C. H., Jr., *Introduction to Physical Gas Dynamics*, 1st ed., Krieger, Malabar, FL, 1986, p. 47.

[17] Goodman, F. O., and Wachman, H. Y., *Dynamics of Gas-Surface Scattering*, Academic Press, New York, 1976, pp. 23–24.

[18] Kuhlthau, A. R., and Bishara, M. N., "On the Nature of the Surface Interaction between Inert Gas Molecules and Engineering Surfaces," *Rarefied Gas Dynamics*, edited by J. H. de Leeuw, Vol. 2, 1966, pp. 518–535.

[19] Woronowicz, M. S., and Rault, D. F. G., "Cercignani–Lampis–Lord Gas–Surface Interaction Model: Comparisons Between Theory and Simulation," *Journal of Spacecraft and Rockets*, Vol. 31, No. 3, 1994, p. 532.

[20] Vanderplaats, G., and Goleta, C., *Design Optimization Tools (DOT) User's Manual*, Ver. 4.20, Vanderplaats Research and Development, Inc., April 1995.

[21] Arora, J. S., *Introduction to Optimum Design*, 1st ed., McGraw–Hill, New York, 1989, pp. 412–414.

[22] Bowman, D. S., "Numerical Optimization of Low-Perigee Spacecraft Shapes," M.S. Thesis, Dept. of Aerospace Engineering, Univ. of Maryland, College Park, MD, May 2001.

J. C. Taylor
Associate Editor